

# Liquid-Liquid Nanogenerator basing on Aqueous-Aqueous Interface

**Long-Long Jiang**

Qingdao University

**Ye Lu**

Qingdao University

**Yang Yu**

College of Physics, Qingdao University

**Dehua Wang**

College of Physics, Qingdao University

**Han Hu**

China University of Petroleum (East China) <https://orcid.org/0000-0002-3755-7342>

**Yang Liu**

Microsystem and Terahertz Research Center, China Academy of Engineering Physics

**Jing Yu**

University of Science and Technology of China

**Jun Zhang**

College of Physics, Qingdao University

**Qingming Ma**

School of Pharmacy, Qingdao University

**Xiaoxiong Wang** (✉ [wangxiaoxiong69@163.com](mailto:wangxiaoxiong69@163.com))

Qingdao University

---

## Article

**Keywords:** liquid-liquid nanogenerator, aqueous two-phase system, immiscible aqueous-aqueous interface, repeatable contact-separation electrification, liquid electronic device

**Posted Date:** November 10th, 2021

**DOI:** <https://doi.org/10.21203/rs.3.rs-1039042/v1>

**License:** © ⓘ This work is licensed under a Creative Commons Attribution 4.0 International License.

[Read Full License](#)

---

**Version of Record:** A version of this preprint was published at Nature Communications on September 9th, 2022. See the published version at <https://doi.org/10.1038/s41467-022-33086-2>.

# Liquid-Liquid Nanogenerator basing on Aqueous-Aqueous Interface

**Jiang Longlong<sup>a†</sup>, Lu Ye<sup>a†</sup>, Yu Yang<sup>a</sup>, Wang Dehua<sup>a</sup>, Hu Han<sup>d</sup>, Liu Yang<sup>e,f</sup>, Yu Jing<sup>g</sup>,  
Zhang Jun<sup>a</sup>, Ma Qingming<sup>b\*</sup>, Wang Xiaoxiong<sup>ach\*</sup>**

<sup>a</sup>. College of Physics, Qingdao University, Qingdao 266071, China

<sup>b</sup>. School of Pharmacy, Qingdao University, Qingdao 266071, China

<sup>c</sup>. Collaborative Innovation Center for Eco-Textiles of Shandong Province, and State Key Laboratory of Bio-Fibers and Eco-Textiles, Qingdao University, Qingdao 266071, China

<sup>d</sup>. State Key Laboratory of Heavy Oil Processing, College of Chemical Engineering, China University of Petroleum(East China), Qingdao 266580, China

<sup>e</sup>. Microsystem and Terahertz Research Center, China Academy of Engineering Physics, Chengdu 610200, China

<sup>f</sup>. Institute of Electronic Engineering, China Academy of Engineering Physics, Mianyang 621999, China

<sup>g</sup>. School of Physics and Electronics, Shandong Normal University, Jinan 250014, China

<sup>h</sup>. University-Industry Joint Center for Ocean Observation and Broadband Communication, College of Physics, Qingdao University, Qingdao 266071, China

<sup>†</sup>These authors contribute equally to this work.

\*Corresponding authors: wangxiaoxiong69@163.com and maqm2012@hotmail.com

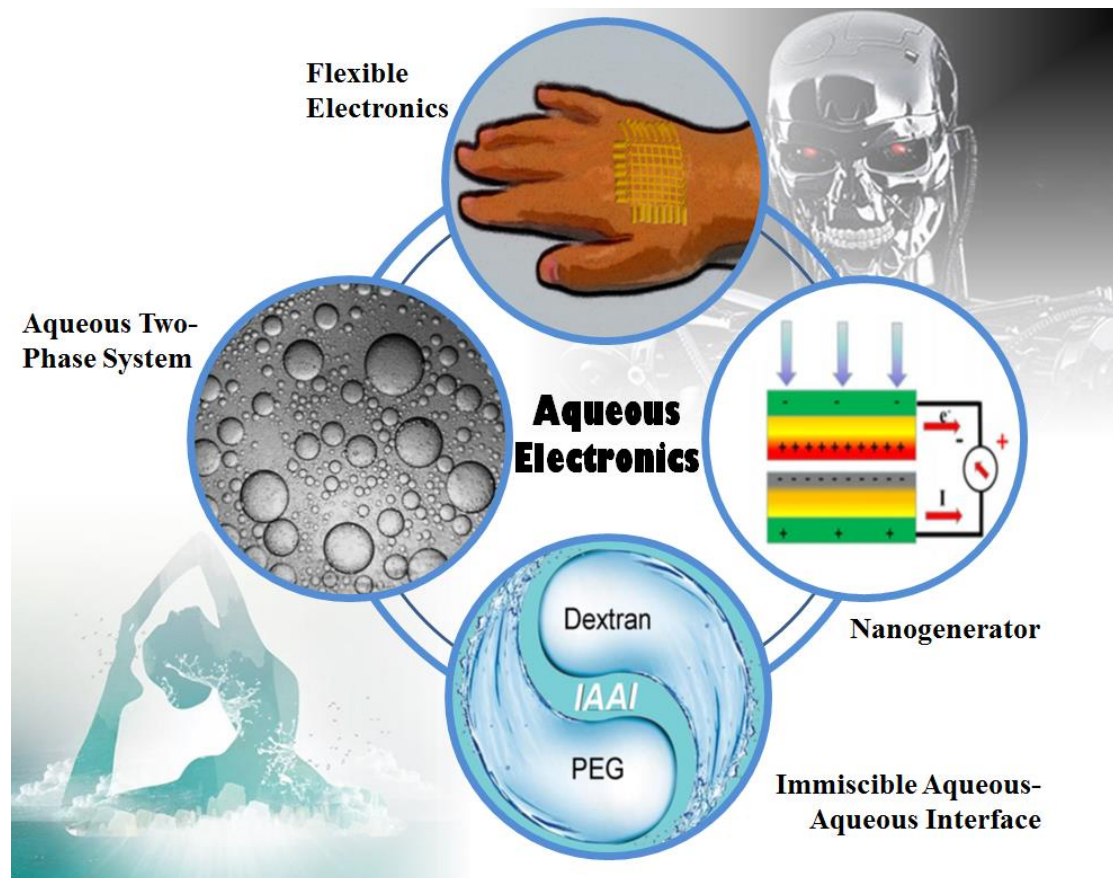
## Abstract

Solid nanogenerators often have a limited charge transfer due to the low contact area. Compared with solid-solid or solid-liquid nanogenerators, liquid-liquid nanogenerators can effectively increase the transferred charge. Limited by the fluidity of the liquid, the precise manipulation of the liquid morphology remains a challenge. In this work, using the surface tension of the droplet to fix the shape, we designed a new liquid-liquid triboelectric nanogenerator by using the immiscible aqueous-aqueous interface, achieving the contact surface charge transfer of 129 nC of a single droplet. This liquid-liquid nanogenerator has been proven to be applicable in humid environments, and the two-phase materials have good biocompatibility and can be used as a good carrier for drugs. Therefore, this nanogenerator is useful for future design of implantable devices and the design of a new type of bionic fully self-powered system has great potential. Meanwhile, such design established the foundation of aqueous electronics and more creation can be achieved by using this route.

**Keywords:** liquid-liquid nanogenerator; aqueous two-phase system; immiscible aqueous-aqueous interface; repeatable contact-separation electrification; liquid electronic device

## Highlights

1. Contact-separation mode liquid-liquid nanogenerator based on aqueous-aqueous interface, and this nanogenerator can achieve repeatable output.
2. The charge transfer of this nanogenerator has reached 129 nC for a single droplet, which exceeds that of the liquid-solid nanogenerator.
3. The new liquid-liquid nanogenerator was found to have an output power density of 0.7 W/m<sup>2</sup>. Considering that the electrochemical window is limited to an output voltage of 0.5 V, the output power density of this system can be rapidly increased by increasing the electrochemical window in the future.
4. The output does not decrease in a humid environment. The good biocompatibility and drug loading provide an important foundation for the application of this nanogenerator in the field of implantable devices.



# 1. Introduction

Nanogenerator (NG) is a new type of distributed energy<sup>1,2,3,4</sup>. According to the principle of energy conversion, nanogenerator can be divided into various categories, including piezoelectric nanogenerators (PENG)<sup>5, 6, 7, 8, 9</sup>, triboelectric nanogenerators (TENG)<sup>10, 11, 12, 13, 14, 15</sup>, and pyroelectric nanogenerators (PyENG)<sup>16, 17, 18, 19</sup>. Among them, TENG has received significant scientific interests due to its unique characteristics like larger output energy<sup>20</sup>. The contact separation mode of TENGs provides important repeatable and quantitative research scheme. In general, the basic working principle of TENG relies on the displacement current induced by the charge, whose energy output depends on the enlargement of the microscopic contact area on the interfaces and the subsequent increase of the interface electron that cloud overlap and generate larger charge transfer<sup>21, 22, 23, 24</sup>. Traditional TENGs are typically designed basing on the solid-solid interface<sup>10, 25, 26, 27</sup>. Recently, nanogenerators basing on the solid-liquid interface have attracted increasing attentions<sup>28, 29, 30</sup>. However, it is difficult to achieve 100% contact by either the solid-solid or the solid-liquid interface, prohibiting the practical applications of TENG. While by using liquid-liquid interface, 100% contact can be easily achieved in a relatively straightforward manner, which shows great promises in developing a new generation of TENG with effective contact area<sup>31, 32, 33, 34, 35</sup>. Such liquid-liquid nanogenerator (L-L TENG) can make good use of the advantages of interface integrity to achieve a larger output. However, current study of L-L TENG is mainly stayed at an infant stage and far from completion. For instance, the traditional liquid-liquid phase interface is easy to fuse and cannot be effectively separated. Moreover, some existing liquid-liquid control schemes, such as dripping liquid<sup>36</sup>, ferrofluid<sup>37</sup>, and water-oil interface<sup>38</sup>, often have some drawbacks like the inconvenience for quantitative research and difficulties in recoverability. Therefore, more appropriate designs of the working mode are urgent for developing better applicable L-L TENG. The design of new L-L TENG can refer to the original solid-solid nanogenerator, which includes vertical contact-separation mode, lateral sliding mode, single-electrode mode, freestanding mode and electrostatic induction mode, etc<sup>8, 15, 37, 39, 40, 41, 42</sup>. The commonality of the modes is the periodic change of the interface capacitance. Therefore, the construction of periodic change of capacitance at the liquid-liquid interface is the basis for the development of more reliable L-L TENGs.

Traditional liquid-liquid interfaces have a relatively high viscosity and it is difficult to achieve effective contact separation between interfaces. In recent years, the newly developed liquid-liquid phase separation control technology based on the all-aqueous systems can be effectively used for reference<sup>43</sup>. Particularly, when two water-soluble polymers, one water-soluble polymer and one salt or two salts are dissolved and mixed at an appropriate concentration and temperature, if the reduction in enthalpy in the system is sufficient to overcome the energy cost associated with the increase in entropy, these different solutes can redistribute in the water and trigger phase separation, forming an aqueous two-phase system (ATPS), by which a recoverable immiscible aqueous-aqueous interface (IAAI) can be created<sup>44, 45, 46</sup>. Compared with the traditional water-oil interface, the viscosity and interfacial tension of the IAAI are lower, which can achieve more effective contact separation<sup>46, 47</sup>. Such recoverable interface provides a new platform for the deepen of research in material charge transfer, which benefits future research in NG fields. In addition, the ATPS can avoid the use of oily phases, organic solvents, strong acids and alkalis with poor biocompatibility, thus can provide a green all-aqueous environment and endow superior biocompatibility for the entire

research process, which enables the construction of biomimetic nanogenerators.

In this work, a new IAAI control case was demonstrated as a novel type of TENG. Such L-L TENG can supply power to an external circuit in series. The construction of IAAI and the design of controlled electronic devices provide an important example for the design of new liquid-phase electronic devices in the future. Based on this interface, more detailed research can be developed to gain a better view in charge behavior by the liquid-liquid interface.

## **2. Materials and Methods**

### **2.1 Materials**

Raw materials are polyethylene glycol (PEG, Mw 8000, Sigma Aldrich Chemical Co., St. Louis, USA), dextran (DEX Mw 500 000, Shanghai Ryon Biological Technology Co. Ltd, Shanghai, China), copper sulfate pentahydrate (Aladdin Chemistry Co. Ltd, Shanghai, China), bull serum albumin (BSA protein) (Sigma-Aldrich Chemical Co., St. Louis, USA), teicoplanin (Aladdin Chemistry Co. Ltd, Shanghai, China), phosphate buffered saline solution (PBS, Aladdin Chemistry Co. Ltd, Shanghai, China), methyl thiazolyl tetrazolium (MTT, Aladdin Chemistry Co. Ltd, Shanghai, China), rhodamine B (Aladdin Chemistry Co. Ltd, Shanghai, China), sodium hydroxide (NaOH, Sinopharm Chemical Reagent Co., Ltd. Shanghai, China), and they are used without further purification. RPMI-1640 Medium and Calcein-AM/PI living/dead cell double staining kit were purchased from Beijing Solarbio Science & Technology Co., Ltd. L929 fibroblasts were purchased from Sigma-Aldrich.

### **2.2 PEG and DEX droplet acquisition method**

An appropriate amount of PEG was weighted and dissolved into 50 g of deionized water, and then an appropriate amount of DEX was slowly added in batches. After the DEX was completely dissolved, the entire solution sample was allowed to stand for 12 h, and obvious layering occurred. The upper layer was the PEG solution, and the lower layer was the DEX solution. The two solutions were taken out separately for further use.

### **2.3 Materials Characterization**

The infrared absorption spectra of PEG and DEX powder, solution and dried powder were obtained by Fourier Transform Infrared Spectroscopy (FTIR, Thermo Scientific Nicolet iN10). The viscosity and interfacial tension of PEG solution and DEX solution were measured by using a spinning drop tensiometer (KRUSS GmbH, Germany) and a rolling ball viscosimeter (Haake-GmbH, Germany), respectively. The contact and separation state of PEG solution and DEX solution was recorded by (Digital Microscope).

The output current signal of L-LTENG was recorded by picoammeter (Keithley 6485), current amplifier (SR 570) and digital oscilloscope (GDS-2102, Gwinstek). The output voltage signal was recorded by a digital oscilloscope (GDS-2102, Gwinstek). The charging voltage of the capacitor was measured by a digital multimeter (Rigol DM 3058).

### **2.4 Biocompatibility**

#### **2.4.1 Cytotoxicity**

The cytotoxicity of DEX&PEG was evaluated by culturing L929 cells. L929 cells were seeded into 96-well plates with  $1 \times 10^4$  cells per well and cultured in 100  $\mu$ L RPMI-1640 medium for 24 h. DEX&PEG were dissolved in RPMI-1640 medium to prepare the sample medium. The sample medium was then filtered with a membrane (0.22  $\mu$ m) to ensure sterility. Subsequently, cells were respectively incubated with normal medium as control group and sample medium as test group for

48 h in 96-well plates. After washing the plate with PBS, MTT (5 mg/mL) in RPMI-1640 (10%) medium was added to each well. After 4 h incubation, each well was washed with PBS to remove the old medium and DMSO was added to dissolve formazan crystals. The absorbance of every well was read at 570 nm with a microplate. Each process has three replicates. The cell viability is calculated as follows:

$$\text{Cell viability (\%)} = \frac{OD_{test}}{OD_{control}} \times 100\% \quad (1)$$

#### 2.4.2 Fluorescence staining of living cells

Calcein-AM/PI living/dead cell double staining kit was used for living and dead cell level analysis. In brief, L929 cells were inoculated in a 24-well plate ( $2 \times 10^4$  cells/well). Then, the prepared sample medium and the normal medium were injected into the wells containing L929 and incubated for 24 h respectively. After washing with PBS, the L929 was stained in a mixture of Calcein-AM (2  $\mu$ M) and PI (4.5  $\mu$ M). Finally, the state of the cells was observed by fluorescence microscopy.

#### 2.4.3 Antibacterial activity

Staphylococcus aureus (S. aureus) and Escherichia coli (E. coli) were selected as different gram-positive and gram-negative model microorganisms to carry out antimicrobial tests respectively. First, bacterial suspension of  $1 \times 10^4$  CFU/mL was prepared with sterile PBS. Then 5 ml of bacterial suspension was co-cultured with the DEX&PEG and teicoplanin at 37°C for 4 h. Bacterial suspension without DEX&PEG was used as control group. 100  $\mu$ L bacterial suspension was added to the surface of solid agarose medium and spread evenly. After incubation at 37°C for 24 h, colony units on solid agarose were observed and recorded. The antibacterial ratio was calculated by the following formula:

$$\text{Antibacterial Ratio(\%)} = \frac{N_b - N_s}{N_b} \times 100\% \quad (2)$$

where  $N_b$  is the number of bacterial colonies in control group,  $N_s$  is the number of bacterial colonies in the samples.

### 3. Results and discussion

#### 3.1 Material characterization and solution differences

As shown in Figure 1a, the upper droplet was hung on the syringe needle, and the needle worked as an electrode simultaneously. An aluminum foil worked as the other electrode and supported the lower droplet. The syringe was driven by a stepping motor to motivate the droplets up and down periodically to achieve contact and separation of the two droplets. In the initial state (I), the PEG droplet was in contact with the DEX droplet, and there was no current or potential. Due to the difference in surface electron affinity, the charge (electron or ion) was transferred from the surface of the PEG droplet to the surface of the DEX droplet, leaving a net positive charge on the surface of the PEG droplet and a net negative charge on the surface of the DEX. When separating, in case the electron can flow through external circuit (state (II)), the resulting charge separation will induce a potential difference on the electrodes, causing subsequent current flow. At the maximum separation distance, the positive current was reduced to zero (III). When the two charged surfaces contact again, the current reverses<sup>48, 49, 50</sup>. Without any contact, no charge is transferred.

In order to characterize the droplet morphology and the compatibility of the L-L TENG when it is working, an optical microscope was used to monitor the three periods before, during and after the contact separation, as shown in Figure 1b. It can be clearly seen that the size and morphology of the

droplets before and after the contact and separation did not change much, and the color of the DEX droplets did not change. (Video S1). This demonstrates that the droplets did not dissolve with each other during the contact and separation. In order to further verify the compatibility of PEG and DEX solution, DEX dyed with rhodamine B dye was added dropwise to PEG solution, as shown in Figure 1c, and compared with dyed deionized water droplets added to pure water, as shown in Figure 1d. When the dyed droplets enter the water and rapidly dissolve into one single phase and diffuse, while DEX droplet enters the PEG solution, there was no color diffusion phenomenon. Due to the density difference, the DEX droplet slowly dropped to the bottom of the test tube, and obvious delamination occurs, resulting in a stable IAAI. (Video S2). This provides sufficient support for the PEG and DEX contact separation movement that does not appear to dissolve with each other.

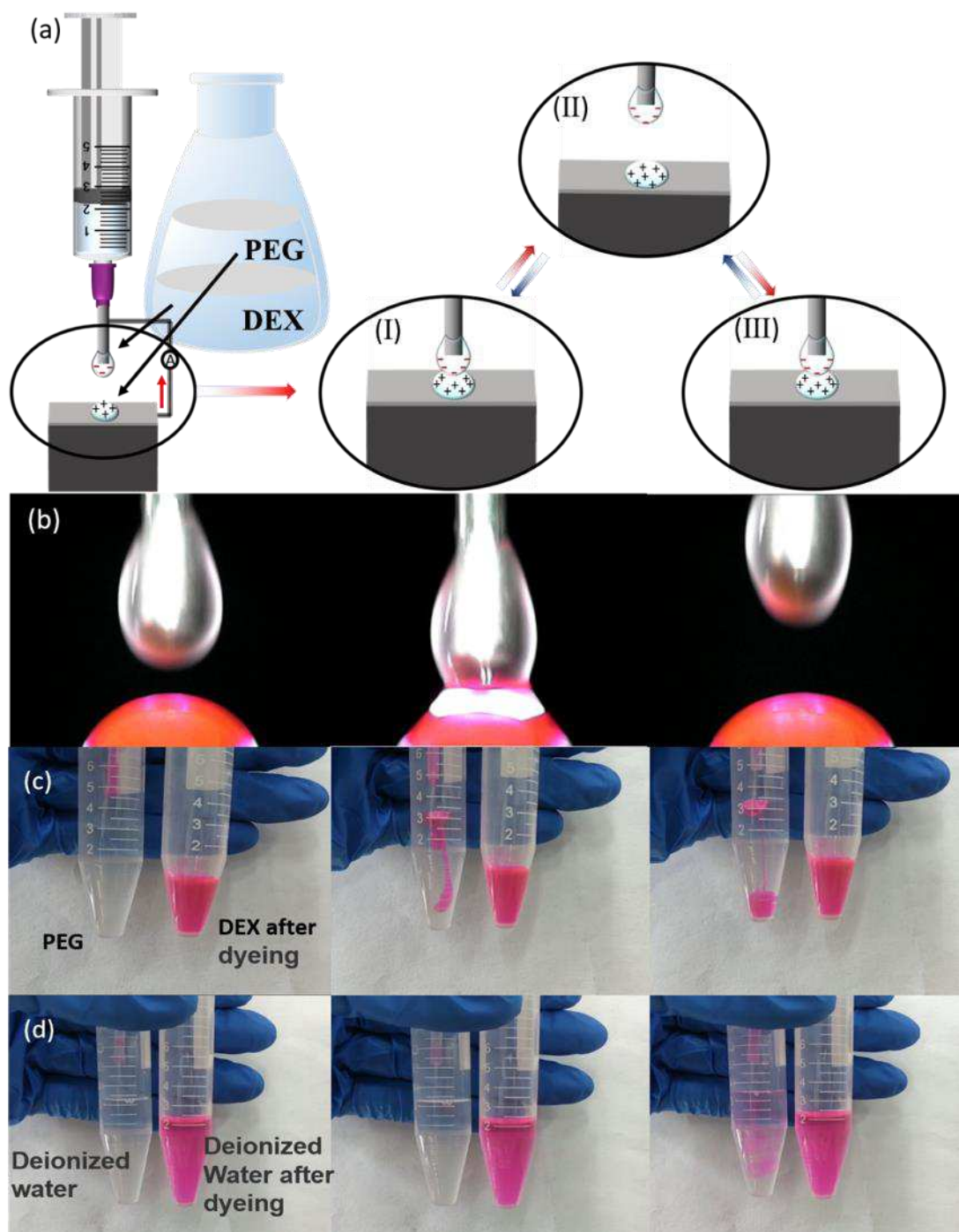


Figure 1: (a) Contact-separation working mode of the L-L TENG. (b) DEX droplet and dyed PEG droplet contact and separate optical image. (c) Image of dyed DEX dripped into PEG to form an IAAI. (d) The optical image of the dyed deionized water dripped into undyed deionized water without the formation of IAAI.

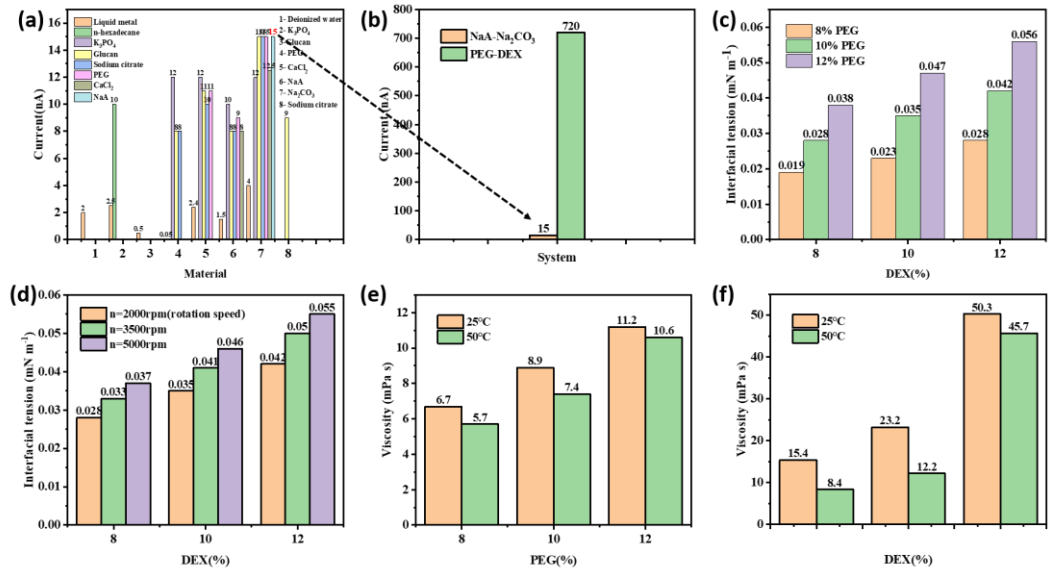


Figure 2: (a) The output signal of contact separation of multiple liquid systems. (b) The output contrast between the PEG-DEX system and the NaA-Na<sub>2</sub>CO<sub>3</sub> system. (c) Surface tension variation with the liquid concentration. (d) Rotating speed affection on the the surface tension of DEX when the PEG concentration is 10%. (e) Temperature variation of PEG viscosity. (f) Temperature variation of DEX viscosity.

Contact-separation electrification performance of a series of liquids were tested to determine the best one. Although some liquids would dissolve or react when contacted (as shown in Table 1 of supporting information Table 1), there was still a current signal. Figure 2a shows the short-circuit current signal generated by the contact and separation of selected different liquids under the same condition. It can be clearly seen that the maximum short-circuit current signal of the other liquid pairs is 15 nA. However, the output signal of the PEG-DEX pair prepared by APTS was about 48 times that of the previous combination. As shown in Figure 2b. It can be speculated that the immiscibility of the two droplets may have relationship with larger amount of charge transfer.

The L-L TENG droplets were characterized for better understanding of the system. The surface tension and viscosity of PEG and DEX were tested using the hanging drop method and rolling ball method, respectively. In the two-phase PEG-DEX system, when the concentration of DEX is constant, the surface tension of PEG increases with the increase of PEG concentration; when the concentration of PEG is constant, the surface tension of DEX increases with the increase of DEX concentration, as shown in Figure 2c. At the same time, the surface tension measured by the hanging drop method can be affected by the rotational speed. Therefore, when the PEG concentration is 10%, the surface tension of different proportions of DEX at different speeds was tested. As shown in Figure 2d, it can be seen that when the concentration of DEX is constant, the surface tension of DEX gradually increases with the increase of the rotation speed; when the rotation speed is constant,

the surface tension of DEX increases with the increase of the concentration. In summary, it can be seen that the surface tension of PEG and DEX is mainly affected by their concentration. In order to further characterize the PEG and DEX in this system, the viscosity of PEG and DEX was tested, as shown in Figure 2e and f. At the same temperature, the viscosity of PEG (DEX) increases as the concentration of PEG (DEX) increases; at the same time, when the concentration of PEG (DEX) is constant, the increase in temperature will cause the drop of the viscosity of PEG and DEX. Because the DEX droplet is suspended on the syringe needle, it is not easy to fall off, and the viscosity is required to be large. At the same time, in order to maintain the integrity of the interface when the droplet contact and separation, the surface tension of the droplet is required to be as large as possible. Therefore, a PEG-DEX (10%-10%) system with moderate surface tension and viscosity was selected for further research. Unless otherwise specified, the L-L TENG tests were all PEG-DEX (10%-10%) systems, tested at room temperature. Infrared spectroscopy was used to characterize the surface chemical bonds of PEG and DEX powders, solutions, and products after the solutions were dried, and the influence of dissolution was analyzed. As shown in Figure S1a, before the dissolution step, characteristic absorption bands of PEG were observed at  $2876\text{ cm}^{-1}$ ,  $1465\text{ cm}^{-1}$ , and  $1113\text{ cm}^{-1}$ , which correspond to  $-\text{CH}_2-$  symmetrical contraction vibration,  $-\text{CH}_2-$  bending vibration, and COC flexural vibration, respectively. After the PEG dissolved, the absorption bands at  $3419\text{ cm}^{-1}$ ,  $1645\text{ cm}^{-1}$ , and  $1113\text{ cm}^{-1}$  can be attributed to  $-\text{OH}$  stretching vibration,  $-\text{OH}$  bending vibration, and COC bending vibration, respectively. The main difference is that the intensity of the  $-\text{OH}$  peak is significantly increased. This shows that PEG is dissolved in deionized water. In the dried product, peaks corresponding to  $-\text{CH}_2-$  symmetrical contraction vibration,  $-\text{CH}_2-$  bending vibration, and C-O-C bending vibration appeared again, indicating that the PEG was not destroyed. As shown in Figure S1b, before the dissolution step, characteristic absorption bands of DEX were observed at  $3419\text{ cm}^{-1}$  and  $1013\text{ cm}^{-1}$ , which correspond to the  $-\text{OH}$  stretching vibration absorption peak and the variable-angle vibration absorption peak of alcoholic hydroxyl groups, respectively. After dissolving DEX, the absorption bands at  $3419\text{ cm}^{-1}$ ,  $1645\text{ cm}^{-1}$ , and  $1013\text{ cm}^{-1}$  can be attributed to  $-\text{OH}$  stretching vibration,  $-\text{OH}$  bending vibration, and variable-angle absorption vibration peaks of alcoholic hydroxyl groups. The main difference is the  $-\text{OH}$  peak. The strength of PEG peaks was significantly increased, indicating that PEG was dissolved in deionized water. In the dried product, the  $-\text{OH}$  stretching vibration absorption peak and the variable angle vibration absorption peak of the alcohol hydroxyl group appeared, indicating that the DEX was not destroyed.

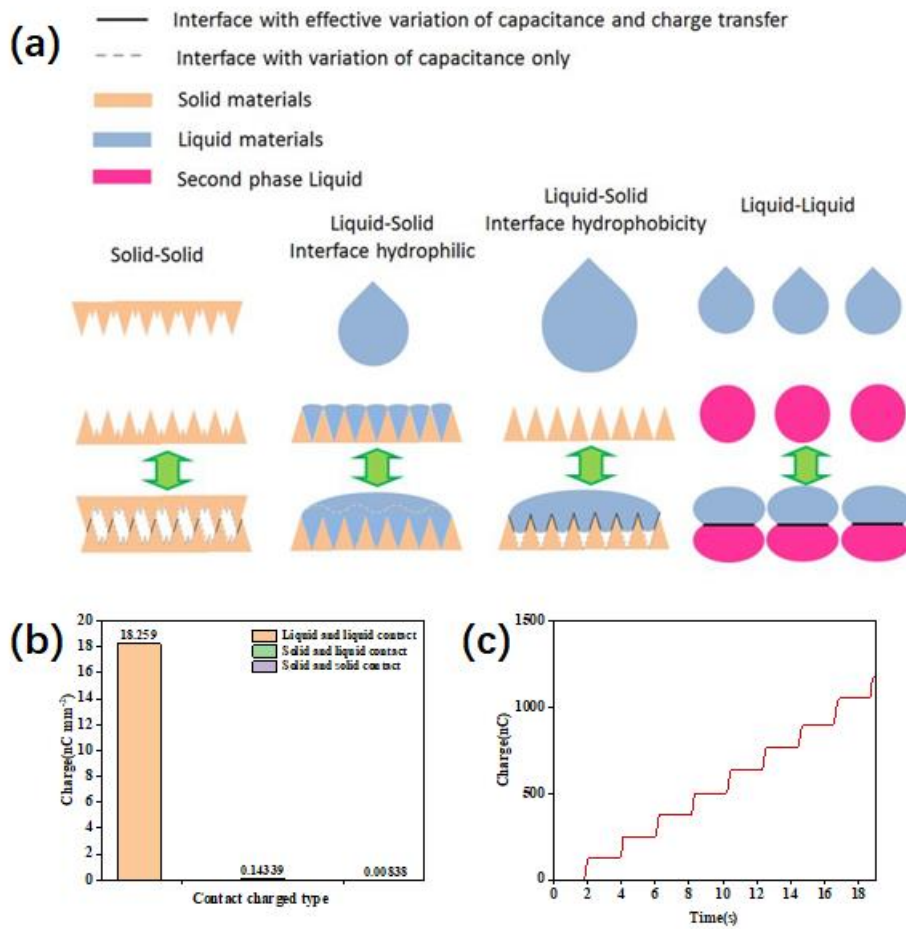


Figure 3: (a) Solid-solid, solid-liquid and liquid-liquid interface contact separation mechanism analysis. (b) Comparison of surface charge density of solid-solid, solid-liquid, and liquid-liquid contact. (c) Transferred charge density of different matter states.

The basic working principle of the triboelectric nanogenerator can be summarized as contact - charge transfer - capacitance change - displacement current induction<sup>51</sup>. The common three states of matter include solid, liquid and gaseous states. Since the capacitance of gas is difficult to manipulate, there are relatively few studies on this type of material in the field of nanogenerators. Therefore, common triboelectric materials include solid-solid, solid-liquid and liquid-liquid. Among them, when solid-solid contacts, only a small fractions of interface area are close enough to achieve charge transfer<sup>22</sup>. The following change in the relative position of the two surfaces causes change of capacitance, inducing displacement current. Pressure may enlarge the working surfaces, but the overall change is small<sup>52, 53, 54</sup>. For the solid-liquid interface, it is divided into hydrophilic and hydrophobic situations. Although the hydrophilic interface can undergo full charge transfer, the subsequent capacitance change interface does not coincide with the charge transfer interface, so it is difficult to induce effective displacement current. For the hydrophobic interface, if the interface is flat enough, the liquid can fully contact the solid, and it can produce a large output; while the common solid interface is not flat enough, the liquid cannot completely form a full interface with the solid, which causes the charge transfer interface to be unsatisfactory<sup>55, 56</sup>. For the L-L TENG, if the liquid can be effectively separated, the charge transfer can be effectively realized on the droplet

interface, and full interface for charge transfer can be achieved, where the effective capacitance variation can be achieved. Such contact benefit can be conveniently utilized in the future for the design of other electronic devices such as recoverable p-n junctions. In order to easily determine the charge transfer effects on different interfaces, a simple comparison experiment was developed, in which nylon-PVDF was used for solid-solid contact, water droplet-PTFE was used for solid-liquid contact, and DEX-PEG aqueous solution pair was used for liquid-liquid contact. As can be seen from Figure 3(b), for the corresponding charge transfer amount, liquid-liquid contact corresponds to scale of  $\times 10 \text{ nC/mm}^2$  level, and liquid-solid contact corresponds to scale of  $\times 0.1 \text{ nC/mm}^2$  level. The solid-solid contact corresponds to the scale of  $\text{pC/mm}^2$  level, which is consistent with the contact interface analysis. Figure 3(c) shows the repeated charge transfer steps of the L-L TENG.

### 3.2 Electrical performance analysis and simulation

In order to characterize the output performance of the PEG-DEX L-L TENG (upper drop  $10 \text{ }\mu\text{L}$ , lower drop  $100 \text{ }\mu\text{L}$ ), a series of electrical signals were tested systematically. As shown in Figure 4a and b, the open circuit voltage and short circuit current can reach  $720 \text{ nA}$  and  $0.41 \text{ V}$ . The relationship between the output signal and the load resistance in the circuit is systematically studied. As shown in Figure 4c, as the load resistance increases, the voltage shows an increasing trend, while the current shows an opposite relationship. We use the formula  $P=U^2/R$  to get the power curve, where the maximum load power density reaches  $0.68 \text{ W/m}^2$ , and the external load resistance is  $200 \text{ K}\Omega$ , as shown in Figure 4d. At maximum power density, the relative load voltage can reach  $0.215 \text{ V}$ , and the relative load current can reach  $480 \text{ nA}$ . Compared with other L-L TENG, the contact-separation mode showed superior output performance and stability, as compared in Table 2 in the supporting information. When the external load is the same as the inherent impedance of TENG<sup>57, 58</sup>, the maximum power transfer occurs, which provides a certain theoretical basis for practical applications. In addition, TENG's pulse energy can be stored in capacitors. Figure 4e shows that commercial capacitors of  $47 \text{ }\mu\text{F}$ ,  $100 \text{ }\mu\text{F}$ , and  $330 \text{ }\mu\text{F}$  can be charged to  $0.34 \text{ V}$ ,  $0.25 \text{ V}$ , and  $0.16 \text{ V}$  at ambient humidity of about  $45^\circ$  and room temperature.

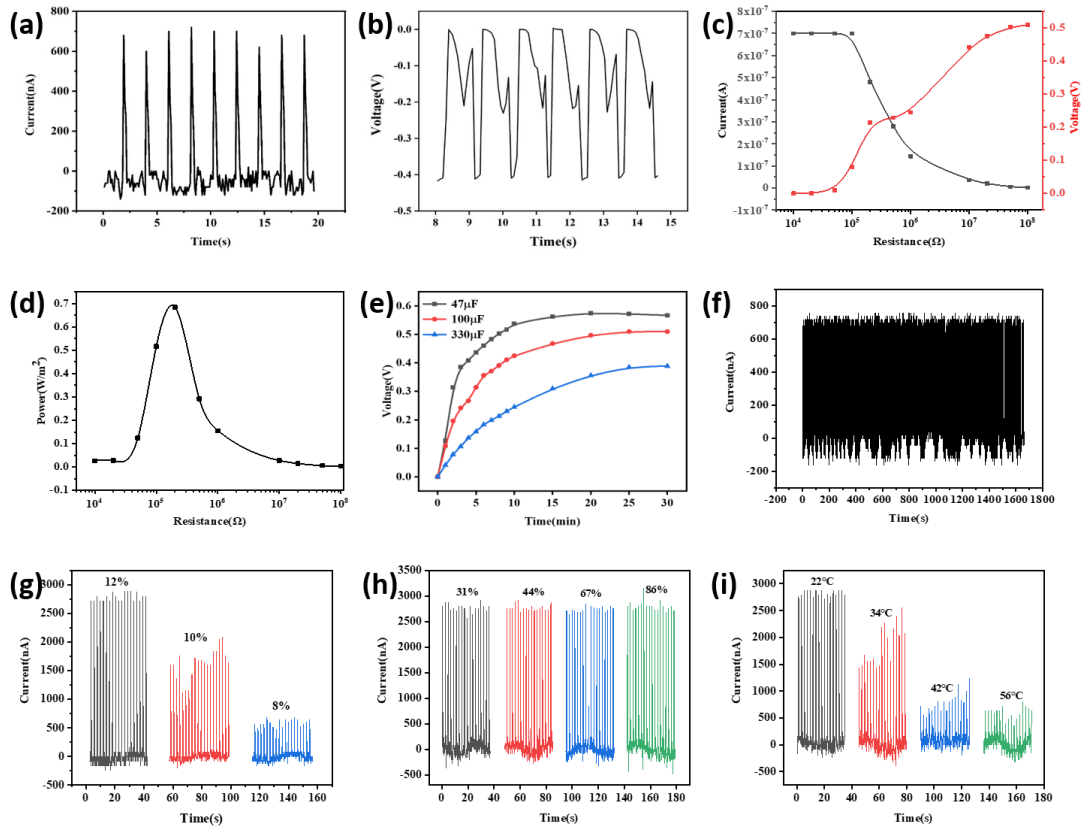


Figure 4: (a) Short-circuit current of the L-L TENG. (b) Open circuit voltage of the L-L TENG. (c) The electric output variation of L-L TENG with the load change. (d) The relationship between the power density of the L-L TENG and the load resistance. (e) The charging curve of commercial capacitors of 47  $\mu\text{F}$ , 100  $\mu\text{F}$ , and 330  $\mu\text{F}$  by the L-L TENG. (f) The repetitive cycle test of the L-L TENG over 1600 s. (g) When the PEG concentration is constant, the relationship between the output current signal of the L-L TENG and the DEX concentration. (h) The output performance of the L-L TENG under different environmental humidity. (i) The output performance of the L-L TENG under different environmental temperature.

In practical applications, the long-term stability/reliability of nanogenerators is a very important issue. Under the same operating conditions, the output performance of the L-L TENG was tested for more than 1600 s. As shown in Figure 4f, the short-circuit current does not decrease, which shows the good stability and durability of the L-L TENG. In order to evaluate the adaptability of the L-L TENG to the environment, the output of the L-L TENG of different concentration PEG-DEX (10%-8%, 10%, 12%), in different ambient humidity and ambient temperature were tested. As shown in Figure 4g, as the DEX concentration decreases, the short-circuit current of the L-L TENG gradually decreases. This may be related to the increase in DEX surface tension and viscosity. In the traditional nanogenerator, the environmental humidity can weaken the triboelectric effect and shorten the storage time of the triboelectric charge on the surface. However, according to Figure 4h, the short-circuit current of the L-L TENG does not change significantly under different environmental humidity conditions. This is due to the incompatibility between DEX and water. The attachment of micro-droplets to DEX droplets does not change the DEX surface concentration. On the contrary, it can infiltrate the surface of the droplets to prevent the water from volatile and solidify,

which is beneficial to prolong the life of the L-L TENG. This makes the L-L TENG work better in a humid environment than traditional nanogenerators. Figure 4i shows that the short-circuit current of the L-L TENG decreases in proportion to the increase in temperature. This is because as the temperature rises, the viscosity of the droplet decreases, the integrity of the interface decreases, resulting in a decrease in output performance.

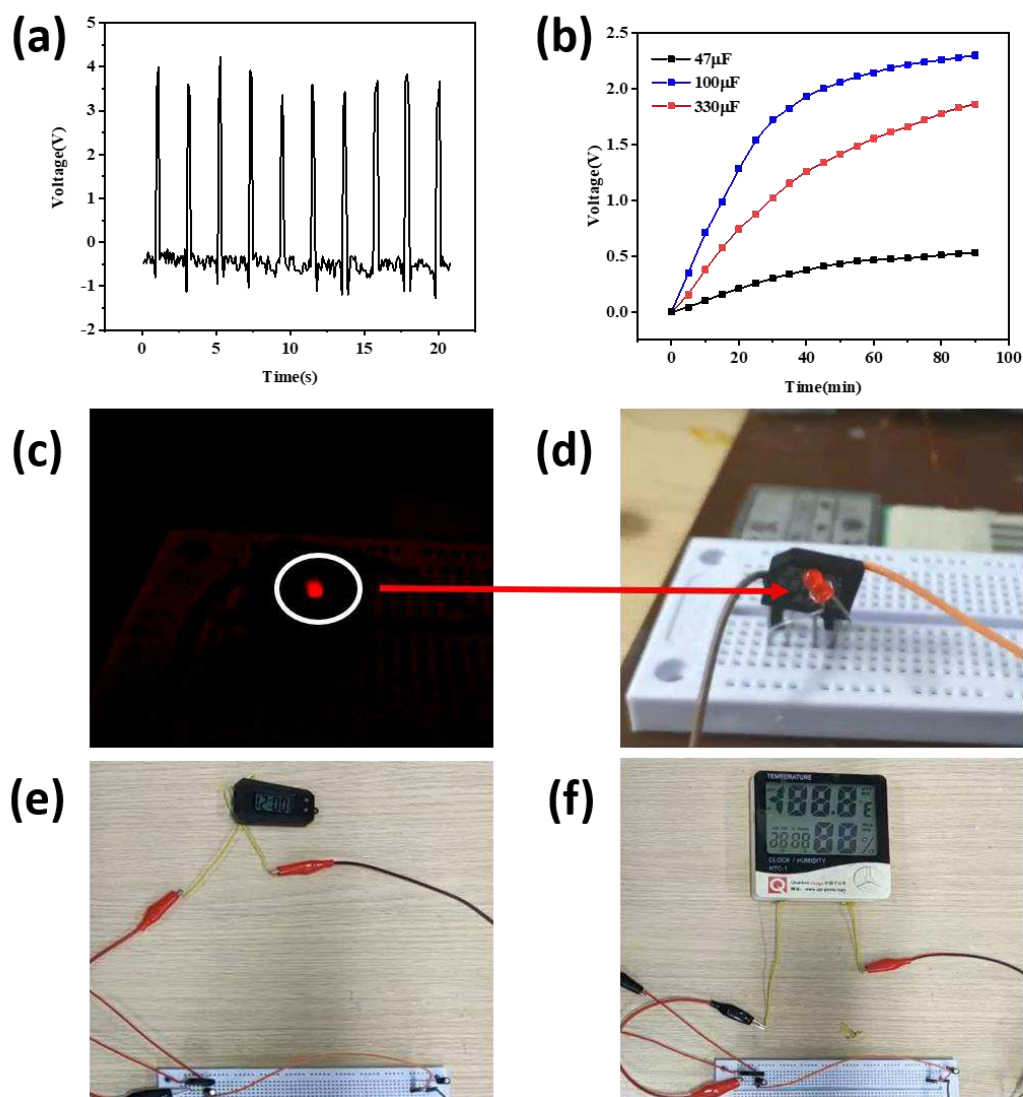


Figure 5: (a) Open circuit voltage generated by the series L-L TENG. (b) charging curve for commercial capacitors of 47  $\mu\text{F}$ , 100  $\mu\text{F}$  and 330  $\mu\text{F}$  respectively. (c), (d) The series L-L TENG can directly light up the LED. The (e) electronic meter and (f) hygrometer can be powered up by the series L-L TENG.

In order to further verify the ability of the L-L TENG as an energy generating device to supply power to small portable smart electronic devices, 10 groups of liquid droplets were connected in series. As shown in Figure 5a, the open circuit voltage can reach 3.92 V after the series connection. Similarly, commercial capacitors of 47  $\mu\text{F}$ , 100  $\mu\text{F}$ , and 330  $\mu\text{F}$  can be charged to 2.3 V, 1.9 V, and 0.5 V respectively, as shown in Figure 5b. As shown in Figure 5c and d, the L-L TENG connected in series can directly light up a single LED under dark conditions. (Video S3). At the same time,

using capacitors and rectifiers, the L-L TENG can also drive the electronic meter (Video S4), as shown in Figure 5e and f. Therefore, this provides a possibility for the L-L TENG to be used in the field of portable self-powered equipment.

For better understanding the working detail of the L-L TENG, finite element analysis was used to simulate a L-L TENG with an ellipse of  $a=0.3$  mm and  $b=0.5$  mm for the upper drop; and an ellipse of  $a=1.5$  mm and  $b=0.5$  mm for the lower drop. As shown in Figures 6a and c, it can be seen that the positive and negative charges generated by the contact and separation of the droplets respectively generate electric potentials of corresponding polarity on the corresponding droplets. The potential difference between the droplets is 0.45 V, which is consistent with the experimental results. In addition, it can be clearly seen that the potential variation scale changes with the separation distance of the droplets during contact separation. The relative potential between the two droplets increases as the droplets approaching each other. When the droplets are closer than 1 cm, the potential difference between the droplets is larger than 0.4 V, as shown in Figure 6b. Simultaneously, the relationship between the surface charge density and the separation distance of the droplets is positively correlated through simulation. As shown in Figure 6d.

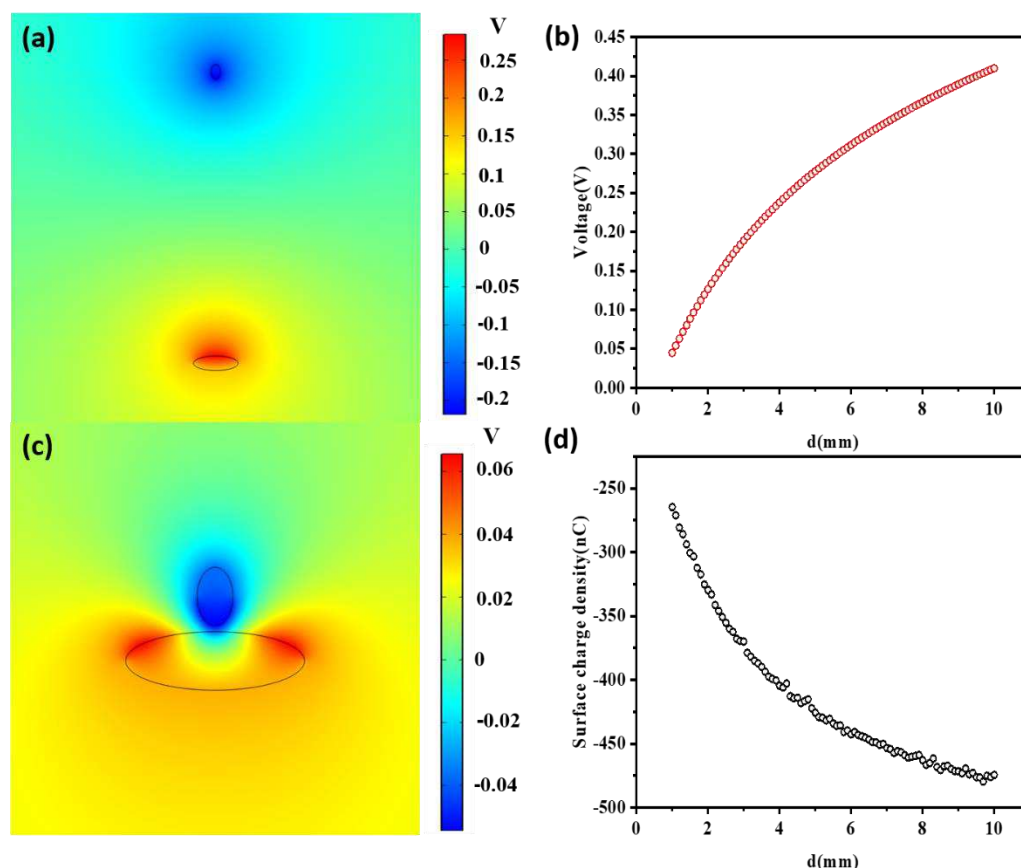


Figure 6: (a), (c) Electric field distribution simulated by finite element analysis. (b) The relationship between the potential difference between two droplets and the separation distance between the droplets. (d) The change in surface charge density caused by the change in the separation distance of the droplet.

### 3.3 Biocompatibility analysis

The aqueous two-phase system (ATPS) is widely used for the separation, purification and enrichment of biomolecules<sup>44, 46, 59, 60</sup>. Making full use of the morphology control ability of this

system can lead to the development of brand-new electronic devices, so the biocompatibility analysis has important value for its future use in implantable device<sup>61</sup>. In order to verify the biocompatibility of the L-L TENG system, the biuret assay and cytotoxicity experiments were conducted. A small amount of BSA protein solution was added to the PEG as the droplets of the L-L TENG. After the L-L TENG works for 0.5 h, the protein-mixed PEG solution was dropped into the 1% CuSO<sub>4</sub>·5H<sub>2</sub>O solution. (Video S5). The original light blue CuSO<sub>4</sub> solution appeared obvious purple after a period, as shown in Figure 7a. This indicates that the BSA protein was not damaged either in PEG solution or during the contact-separation process, demonstrating the good biocompatibility of the L-L TENG for biomolecules. Moreover, the cytotoxicity of material itself is another important index to evaluate the biocompatibility. The cytotoxicity of the DEX&PEG was investigated by a living/dead assay. As illustrated by the fluorescence images in Figure 7b, the number of living cells (green) cultured with DEX&PEG was not significantly reduced and the cell morphology was stable compared to the blank control group. Moreover, there were almost invisible red signals in the microscopic field of view, indicating a particularly low number of dead cells during the culture process. Besides, the cytotoxicity of DEX&PEG was evaluated qualitatively by conducting MTT assay. According to cell viability, cytotoxicity results can be divided into three levels (< 50%, toxic; 51% ~ 70%, low cytotoxicity; > 70%, non-toxic). As shown by the plots in Figure 7c, the cell viability of the DEX&PEG was around 95.14%, indicating that DEX&PEG was obvious non-cytotoxicity. In summary, the DEX&PEG has superior cytocompatibility and biological safety, and can be used as medical materials.

ATPS can gain versatility by loading functional materials, so drug-loading performance was investigated to show the developability of the L-L TENG. *Staphylococcus aureus* (*S. aureus*) and *Escherichia coli* (*E. coli*) are selected as Gram-positive bacteria and Gram-negative bacteria for the bacteriostatic test respectively. As shown by the optical images of the bacterial colonies and the plots in Figure 7d and e, DEX&PEG show no obvious antibacterial activity against *S. aureus* and *E. coli*. Teicoplanin is a recognized antibiotic agent, and its antibacterial ratio against *E. coli* and *S. aureus* was 95.32% and 95.19%, respectively. Compared with teicoplanin, the teicoplanin-loaded DEX&PEG system also show similar antibacterial properties, demonstrating the great potentials of DEX&PEG for future antibacterial applications. In summary, the L-L TENG not only has excellent biocompatibility, but also can load antibacterial drugs as a demonstration of its potential to develop future designs. This is precious for systems that are applicable to living organisms.

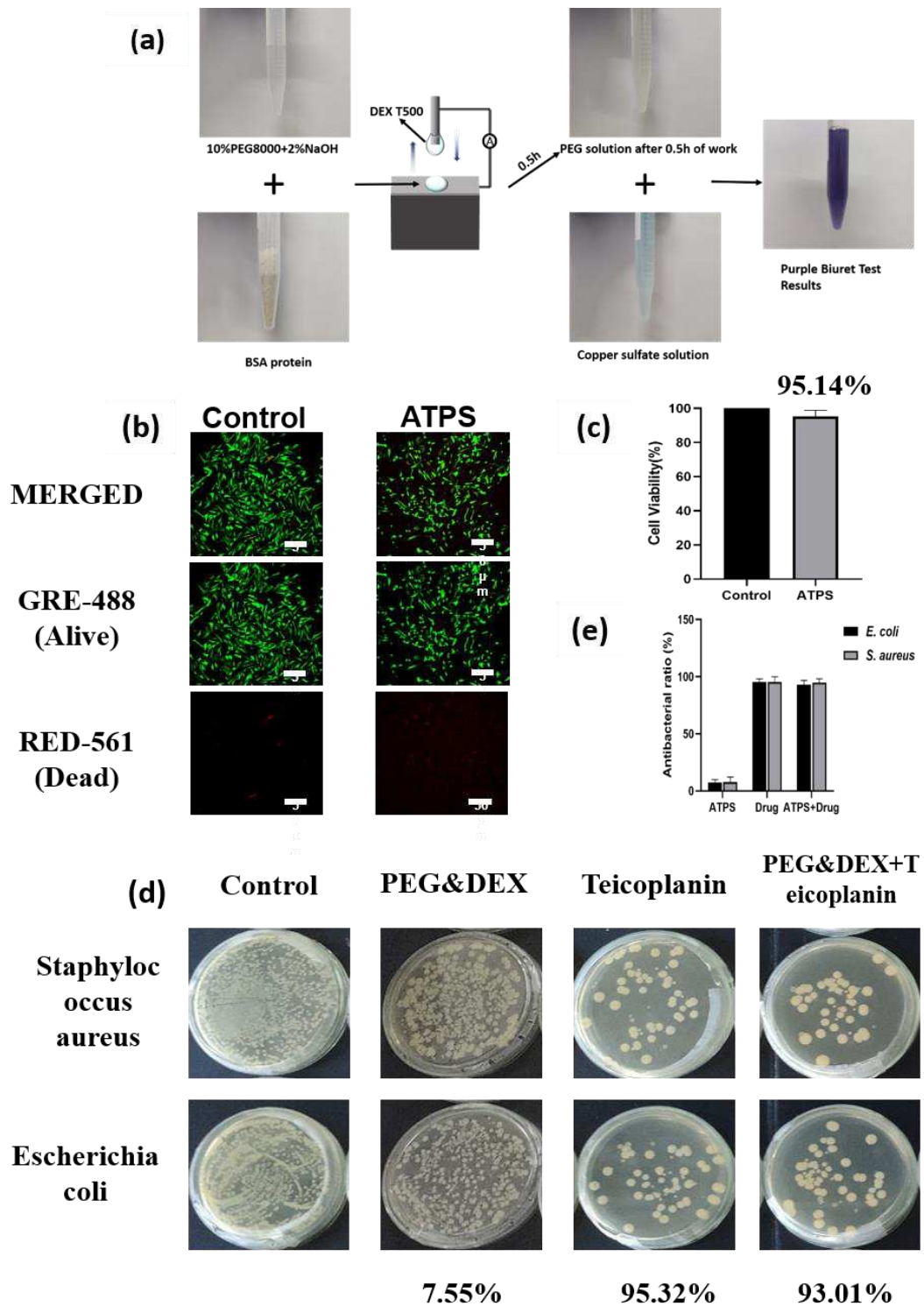


Figure 7: (a) The PEG solution with BSA protein added to the 1%  $\text{CuSO}_4 \cdot 5\text{H}_2\text{O}$  solution before and after the L-L TENG working for 0.5 h. (b) Live/dead cell fluorescence Image. (c) The proportion of living cells in (b). (d) antibacterial experiment of PEG-DEX system loaded with antibacterial drugs. (e) graph (d) histogram of antibacterial rate of antibacterial experiment.

## 4. Conclusion

Using the two-phase immiscible aqueous system, the vertical contact separation L-L TENG was designed, therefore the similar behavior of the repeatable contact-separation can be achieved. The actual output power density of this L-L TENG can reach  $0.7 \text{ W/m}^2$ . The maximum output charge of a single droplet is determined to be 129 nC per droplet, which exceeds the fully charged liquid-solid nanogenerator. The charge density can be attributed to the higher effective contact area of the IAAs<sup>22</sup>. The output performance of this nanogenerator does not decrease in a humid environment. It has good biocompatibility, and can be conveniently loaded with drugs, by which can be used for implantable electronic devices and the like. The actual output of this nanogenerator is limited by the electrochemical window, which is about 0.5 V. In the future, a higher output energy density can be obtained by designing a higher electrochemical window.

## Acknowledgement

This work was supported by the National Natural Science Foundation of China (12104249, 22008130, 11904214, 11804313 and 11847135), Shandong Provincial Natural Science Foundation (ZR2020KA004), the Youth Innovation Team Project of Shandong Provincial Education Department (2020KJN015), State Key Laboratory of Bio-Fibers and Eco-Textiles (Qingdao University), No. KF2020204, GZRC202011 & ZKT46.

1. Fan FR, Tang W, Wang ZL. Flexible Nanogenerators for Energy Harvesting and Self-Powered Electronics. *Advanced Materials* **28**, 4283-4305 (2016).
2. Wang ZL. On Maxwell's displacement current for energy and sensors: the origin of nanogenerators. *Materials Today* **20**, 74-82 (2017).
3. Mariello M, Guido F, Mastronardi VM, Todaro MT, Desmaële D, De Vittorio M. Nanogenerators for harvesting mechanical energy conveyed by liquids. *Nano Energy* **57**, 141-156 (2019).
4. Song W-Z, *et al.* Sliding non-contact inductive nanogenerator. *Nano Energy* **63**, 103878 (2019).
5. Hu D, Yao M, Fan Y, Ma C, Fan M, Liu M. Strategies to achieve high performance piezoelectric nanogenerators. *Nano Energy* **55**, 288-304 (2019).
6. Lu L, Ding W, Liu J, Yang B. Flexible PVDF based piezoelectric nanogenerators. *Nano Energy* **78**, 105251 (2020).
7. Niu X, *et al.* High-Performance PZT-Based Stretchable Piezoelectric Nanogenerator. *ACS Sustainable Chemistry & Engineering* **7**, 979-985 (2019).
8. Wang X, *et al.* Bionic Single-Electrode Electronic Skin Unit Based on Piezoelectric Nanogenerator. *ACS nano* **12**, 8588-8596 (2018).

9. Liu Q, *et al.* Wireless Single-Electrode Self-Powered Piezoelectric Sensor for Monitoring. *ACS Applied Materials & Interfaces* **12**, 8288-8295 (2020).
10. Song Y, Wang N, Wang Y, Zhang R, Olin H, Yang Y. Direct Current Triboelectric Nanogenerators. *Advanced Energy Materials* **10**, 2002756 (2020).
11. Liu W, *et al.* Integrated charge excitation triboelectric nanogenerator. *Nature Communications* **10**, 1426 (2019).
12. Conta G, Libanori A, Tat T, Chen G, Chen J. Triboelectric Nanogenerators: Triboelectric Nanogenerators for Therapeutic Electrical Stimulation *Advanced Materials* **33**, 2170201 (2021).
13. Yan K, *et al.* A non-toxic triboelectric nanogenerator for baby care applications. *Journal of Materials Chemistry A* **8**, 22745-22753 (2020).
14. Qiu H-J, *et al.* A calibration-free self-powered sensor for vital sign monitoring and finger tap communication based on wearable triboelectric nanogenerator. *Nano Energy* **58**, 536-542 (2019).
15. Wang X-X, *et al.* Anisotropic nanogenerator for anticounterfeiting and information encrypted transmission. *Nano Energy* **71**, 104572 (2020).
16. Zhang K, Wang Y, Wang ZL, Yang Y. Standard and figure-of-merit for quantifying the performance of pyroelectric nanogenerators. *Nano Energy* **55**, 534-540 (2019).
17. Ryu H, Kim S-W. Emerging Pyroelectric Nanogenerators to Convert Thermal Energy into Electrical Energy. *Small (Weinheim an der Bergstrasse, Germany)* **17**, 1903469 (2021).
18. Lee J-H, *et al.* Thermally Induced Strain-Coupled Highly Stretchable and Sensitive Pyroelectric Nanogenerators. *Advanced Energy Materials* **5**, 1500704 (2015).
19. You M-H, *et al.* A self-powered flexible hybrid piezoelectric–pyroelectric nanogenerator based on non-woven nanofiber membranes. *Journal of Materials Chemistry A* **6**, 3500-3509 (2018).
20. Wang N, *et al.* Anisotropic Triboelectric Nanogenerator Based on Ordered Electrospinning. *ACS Applied Materials & Interfaces* **12**, 46205-46211 (2020).
21. Zou Y, Xu J, Chen K, Chen J. Triboelectric Nanogenerators: Advances in Nanostructures for High-Performance Triboelectric Nanogenerators *Advanced Materials Technologies* **6**, 2170016 (2021).
22. Liu Y, *et al.* Quantifying contact status and the air-breakdown model of charge-excitation triboelectric nanogenerators to maximize charge density. *Nature Communications* **11**, 1599 (2020).

23. Lin S, Chen X, Wang ZL. Contact Electrification at the Liquid–Solid Interface. *Chemical Reviews*, (2021).
24. Lin S, Xu C, Xu L, Wang ZL. The Overlapped Electron-Cloud Model for Electron Transfer in Contact Electrification. *Advanced Functional Materials* **30**, 1909724 (2020).
25. Rodrigues C, Gomes A, Ghosh A, Pereira A, Ventura J. Power-generating footwear based on a triboelectric-electromagnetic-piezoelectric hybrid nanogenerator. *Nano Energy* **62**, 660-666 (2019).
26. Singh HH, Khare N. Flexible ZnO-PVDF/PTFE based piezo-tribo hybrid nanogenerator. *Nano Energy* **51**, 216-222 (2018).
27. Qin Z, Yin Y, Zhang W, Li C, Pan K. Wearable and Stretchable Triboelectric Nanogenerator Based on Crumpled Nanofibrous Membranes. *ACS Applied Materials & Interfaces* **11**, 12452-12459 (2019).
28. Wei X, *et al.* All-Weather Droplet-Based Triboelectric Nanogenerator for Wave Energy Harvesting. *ACS nano* **15**, 13200-13208 (2021).
29. Kumar S, Sharma A, Gupta V, Tomar M. Development of novel MoS<sub>2</sub> hydrovoltaic nanogenerators for electricity generation from moving NaCl droplet. *J Alloy Compd* **884**, 161058 (2021).
30. Xu W, *et al.* A droplet-based electricity generator with high instantaneous power density. *Nature* **578**, 392-396 (2020).
31. Gauthier M, *et al.* Electrode–Electrolyte Interface in Li-Ion Batteries: Current Understanding and New Insights. *The Journal of Physical Chemistry Letters* **6**, 4653-4672 (2015).
32. Yu X, Manthiram A. Electrode–electrolyte interfaces in lithium-based batteries. *Energy & Environmental Science* **11**, 527-543 (2018).
33. Xu L, *et al.* Interfaces in Solid-State Lithium Batteries. *Joule* **2**, 1991-2015 (2018).
34. Wu B, Wang S, Evans IV WJ, Deng DZ, Yang J, Xiao J. Interfacial behaviours between lithium ion conductors and electrode materials in various battery systems. *Journal of Materials Chemistry A* **4**, 15266-15280 (2016).
35. Nolan AM, Zhu Y, He X, Bai Q, Mo Y. Computation-Accelerated Design of Materials and Interfaces for All-Solid-State Lithium-Ion Batteries. *Joule* **2**, 2016-2046 (2018).
36. Nie J, Wang Z, Ren Z, Li S, Chen X, Lin Wang Z. Power generation from the interaction of a liquid

droplet and a liquid membrane. *Nature Communications* **10**, 2264 (2019).

37. Wang P, Zhang S, Zhang L, Wang L, Xue H, Wang ZL. Non-contact and liquid–liquid interfacing triboelectric nanogenerator for self-powered water/liquid level sensing. *Nano Energy* **72**, 104703 (2020).
38. Zhao X, *et al.* Studying of contact electrification and electron transfer at liquid-liquid interface. *Nano Energy* **87**, 106191 (2021).
39. Zhang Z, *et al.* Triboelectric nanogenerators with simultaneous outputs in both single-electrode mode and freestanding-triboelectric-layer mode. *Nano Energy* **66**, 104169 (2019).
40. Niu S, *et al.* Theory of freestanding triboelectric-layer-based nanogenerators. *Nano Energy* **12**, 760-774 (2015).
41. Cheedarala RK, Duy LC, Ahn KK. Double characteristic BNO-SPI-TENGs for robust contact electrification by vertical contact separation mode through ion and electron charge transfer. *Nano Energy* **44**, 430-437 (2018).
42. Zhou L, *et al.* Rationally Designed Dual-Mode Triboelectric Nanogenerator for Harvesting Mechanical Energy by Both Electrostatic Induction and Dielectric Breakdown Effects. *Advanced Energy Materials* **10**, 2000965 (2020).
43. Ma Q, *et al.* Cell-Inspired All-Aqueous Microfluidics: From Intracellular Liquid–Liquid Phase Separation toward Advanced Biomaterials. *Advanced Science* **7**, 1903359 (2020).
44. Iqbal M, *et al.* Aqueous two-phase system (ATPS): an overview and advances in its applications. *Biological Procedures Online* **18**, 18 (2016).
45. Grilo AL, Raquel Aires-Barros M, Azevedo AM. Partitioning in Aqueous Two-Phase Systems: Fundamentals, Applications and Trends. *Separation & Purification Reviews* **45**, 68-80 (2016).
46. Chao Y, Shum HC. Emerging aqueous two-phase systems: from fundamentals of interfaces to biomedical applications. *Chemical Society Reviews* **49**, 114-142 (2020).
47. Atefi E, Mann JA, Tavana H. Ultralow Interfacial Tensions of Aqueous Two-Phase Systems Measured Using Drop Shape. *Langmuir* **30**, 9691-9699 (2014).
48. Li Z, Shen J, Abdalla I, Yu J, Ding B. Nanofibrous membrane constructed wearable triboelectric nanogenerator for high performance biomechanical energy harvesting. *Nano Energy* **36**, 341-348 (2017).
49. Chen BD, *et al.* Water wave energy harvesting and self-powered liquid-surface fluctuation sensing based on bionic-jellyfish triboelectric nanogenerator. *Materials Today* **21**, 88-97 (2018).

50. Willatzen M, Lin Wang Z. Theory of contact electrification: Optical transitions in two-level systems. *Nano Energy* **52**, 517-523 (2018).
51. Wang ZL, Jiang T, Xu L. Toward the blue energy dream by triboelectric nanogenerator networks. *Nano Energy* **39**, 9-23 (2017).
52. Yang W, *et al.* Fundamental research on the effective contact area of micro-/nano-textured surface in triboelectric nanogenerator. *Nano Energy* **57**, 41-47 (2019).
53. Kantar E, Hvidsten S, Mauseth F, Ildstad E. A stochastic model for contact surfaces at polymer interfaces subjected to an electrical field. *Tribology International* **127**, 361-371 (2018).
54. Yastrebov VA, Anciaux G, Molinari J-F. From infinitesimal to full contact between rough surfaces: Evolution of the contact area. *International Journal of Solids and Structures* **52**, 83-102 (2015).
55. Montes Ruiz-Cabello FJ, Cabrerizo-Vílchez MA, Rodríguez-Valverde MA. Evaluation of the solid-liquid contact area fraction of drops deposited on rough surfaces beyond the Wenzel regime. *Colloids and Surfaces A: Physicochemical and Engineering Aspects* **568**, 455-460 (2019).
56. Kim YH, Kim K, Jeong JH. Determination of the adhesion energy of liquid droplets on a hydrophobic flat surface considering the contact area. *International Journal of Heat and Mass Transfer* **102**, 826-832 (2016).
57. Li W, Chen T, Xu W. On impedance matching and maximum power transfer. *Electric Power Systems Research* **80**, 1082-1088 (2010).
58. Liao Y, Liang J. Maximum power, optimal load, and impedance analysis of piezoelectric vibration energy harvesters. *Smart Materials and Structures* **27**, 075053 (2018).
59. Seo H, Nam C, Kim E, Son J, Lee H. Aqueous Two-Phase System (ATPS)-Based Polymersomes for Particle Isolation and Separation. *ACS Applied Materials & Interfaces* **12**, 55467-55475 (2020).
60. Souza RL, Ventura SPM, Soares CMF, Coutinho JAP, Lima ÁS. Lipase purification using ionic liquids as adjuvants in aqueous two-phase systems. *Green Chemistry* **17**, 3026-3034 (2015).
61. Wanli Wang, *et al.* Applications of nanogenerators for biomedical engineering and healthcare systems. *InfoMat*, (2021).

## Supplementary Files

This is a list of supplementary files associated with this preprint. Click to download.

- [SI.pdf](#)
- [VideoS1.mp4](#)
- [VideoS2.mp4](#)
- [VideoS3.mp4](#)
- [VideoS4.mp4](#)
- [VideoS5.mp4](#)